MATERIALS CHEMISTRY
FRONTIERS

RESEARCH ARTICLE

View Article Online
View Journal | View Issue

Cite this: *Mater. Chem. Front.*, 2019, **3**, 1653

Metal–organic framework derived hierarchical Ni/Ni_3S_2 decorated carbon nanofibers for high-performance supercapacitors†

Di Tian, Sihui Chen, Wendong Zhu, Ce Wang * and Xiaofeng Lu *

Received 7th May 2019,
Accepted 9th June 2019

DOI: 10.1039/c9qm00296k

rsc.li/frontiers-materials

Metal–organic frameworks (MOFs) and their derivatives have emerged as promising electrode materials in the energy conversion and storage field in the past few years. Herein, hierarchical Ni/Ni_3S_2 decorated carbon nanofibers (CNFs) have been fabricated based on the template growth of MOFs on pre-oxidized electrospun polyacrylonitrile (PAN) nanofibers followed by carbonization and sulfurization processes. The formation of Ni and CNFs provides high conductivity, while the hierarchical structure contributes to a large number of exposed redox active sites. Thus the optimized hierarchical Ni/Ni_3S_2/CNFs achieve a high electrochemical performance as supercapacitor electrodes, exhibiting a specific capacitance of 830.0 F g^{-1} at 0.2 A g^{-1} and ideal rate capabilities. In addition, the assembled solid-state supercapacitor delivers a high energy density of 31.6 W h kg^{-1} at a power density of 1800 W kg^{-1} and a good capacitance retention of 95.7% after 5000 charge–discharge cycles. This strategy provides a basis for the efficient construction of MOF-derived electrode materials for their application in energy storage systems.

Introduction

The growing demand for clean and sustainable energy sources has promoted the development of supercapacitors because of their advantages of high power energy, fast recharge ability, long cycling life, and excellent safety.[1–5] As a vital contributor, a large variety of electrode materials have been prepared to satisfy the requirements of high-performance supercapacitors including large specific capacitance, superior rate capability, excellent stability and huge energy densities. The commonly used single component electrode materials including carbon materials, transition metal oxides and conductive polymers exhibit some advantages in certain aspects, but usually suffer from their respective intrinsic shortcomings. Therefore, designing new types of functional hybrid materials with multiple components and a unique hierarchical structure is necessary to achieve an improved electrochemical performance.

From a chemical point of view, the lower electronegativity of sulfur than oxygen leads to a more stable structure and faster electron transport in metal sulfides than oxides.[6,7] Among a large number of metal sulfides, Ni_3S_2, as a rich and cheap mineral in nature, displays rich valences, large theoretical capacity, and good electrochemical performance, which has been regarded as a remarkable electrode material for energy storage.[8–11] Additionally, in order to further improve the inferior conductivity and enlarge the Faraday active areas of Ni_3S_2 materials, they are usually decorated on highly conductive substrates such as graphenes, carbon nanotubes and carbon nanofibers. There are two common synthetic routes. One is to directly grow Ni_3S_2 on the substrates. For example, a Ni_3S_2 nanoparticles/carbon nanotube hybrid is prepared through a glucose-assisted hydrothermal approach, displaying a high specific capacitance of 800 F g^{-1} at 3.2 A g^{-1} and great cycling stability.[13] The other is to prepare Ni_3S_2 composites using Ni, NiO, $Ni(OH)_2$, *etc.* as precursors. Li and co-workers have synthesized grass-like Ni_3S_2 nanorod/nanowire arrays grown on a Ni foam network, providing a large interfacial area and effective pathway for charge transport, which showed a specific area capacitance of 4.52 F cm^{-2} at 1.25 mA cm^{-2} as supercapacitor electrodes.[12] Compared with the former, the latter is more conducive to the synergy of multi-component or hierarchical structures.

Recently, metal–organic frameworks (MOFs) have been demonstrated as efficient electrode materials for supercapacitors owing to their porous architecture, diverse composition and redox reactivity.[14–17] According to their unique characteristics, some typical MOFs have been directly used as parts or all of electrode materials to provide a large specific surface area and abundant pseudocapacitive sites.[18–21] Furthermore, for the purpose of achieving better conductivity, enhanced structural stability, and specific compositional transformation, a large number of MOF derived electrode materials including carbon

Alan G. MacDiarmid Institute, College of Chemistry, Jilin University, Changchun, 130012, P. R. China. E-mail: cwang@jlu.edu.cn, xflu@jlu.edu.cn; Fax: +86-431-85168292; Tel: +86-431-85168292

† Electronic supplementary information (ESI) available. See DOI: 10.1039/c9qm00296k

materials, oxides and sulfides have aroused increasing attention recently.[22–27] In our previous work, MOF derived Ni doped carbon nanofibers were prepared, which have been used as supercapacitor electrodes to achieve a specific capacitance of 300.0 F g^{-1} at a current density of 0.5 A g^{-1} and good rate capacity. However, the limitation of the active Faraday reactions of the single component, Ni, hindered their capacitance performance.[28] Therefore, it is desirable to convert Ni to Ni_3S_2 with carbon substrates, thus the electrode materials can possess good conductivity, high surface area and excellent redox activity.

In this study, we have demonstrated a novel strategy to fabricate MOF derived hierarchical Ni/Ni_3S_2 decorated CNFs as supercapacitor electrodes through a template growth method followed by carbonization and sulfurization processes. Because of the unique hierarchical structure of Ni/Ni_3S_2 and highly conductive CNFs, the prepared Ni/Ni_3S_2/CNFs show a large redox active area and efficient electron transfer path, guaranteeing their excellent performance in terms of specific capacitance, rate capacity, and cycling stability. As a result, the largest specific capacitance of 830.0 F g^{-1} can be achieved at a current density of 0.2 A g^{-1} with a good rate capacitance retention of 42.4% as the current density increased to 5 A g^{-1}. In addition, an asymmetric supercapacitor is assembled by using Ni/Ni_3S_2/CNFs as the anode material and active carbon as the cathode material, which extend the potential window to 1.8 V *via* the usage of a solid electrolyte, leading to a high energy density of 31.6 W h kg^{-1} at a power density of 1800 W kg^{-1}. Furthermore, the supercapacitor shows a capacitance retention of 93.5% and high Coulombic efficiency after 5000 cycles. The high-performance of the supercapacitor reveals its great potential for practical applications in energy storage and conversion devices.

Experimental

All chemical reagents consisting of polyacrylonitrile (PAN, M_w = 80 000, Jilin Chemical Plant.), *N*,*N*-dimethylformamide (DMF, Beijing Chemical Works), terephthalic acid (H_2BDC, AR, Aladdin Industrial Corporation), nickel nitrate hexahydrate ($Ni(NO_3)_2{\cdot}6H_2O$, AR, Tianjin Tiantai Fine Chemicals Co., Ltd), thioacetamide (AR, Sinopharm Chemical Reagent Co., Ltd), ethanol (EtOH, Beijing Chemical Works), polytetrafluoroethylene (PTFE, Aladdin), potassium hydroxide (KOH, Beijing Chemical Works), and polyvinyl alcohol (PVA, $M_w \approx$ 77 000, Beijing Yili Fine Chemical Co., Ltd) were used as received without further purification. The water used in the experiment refers to ultrapure water.

Synthesis of MOF derived Ni/CNFs

The fabrication of MOF derived Ni/CNFs was similar to that in our previous report.[28] In brief, $Ni(NO_3)_2{\cdot}6H_2O$ (1.164 g) and H_2BDC (0.168 g) were completely dissolved in DMF (25 mL) to form a transparent greenish solution. Then pre-oxidized polyacrylonitrile nanofibers (PPNFs, 10 mg) prepared by an electrospinning and calcination process at 240 °C were immersed in the above solution for 20 h and transferred into a Teflon-lined stainless-steel autoclave (50 mL) at 120 °C for 16 h. After washing with water and ethanol and drying, the obtained PPNF@MOF was carbonized at a high temperature in an Ar atmosphere to produce Ni/CNFs. The samples fabricated at carbonization temperatures of 500, 700 and 900 °C were designated as Ni/CNFs-500, Ni/CNFs-700 and Ni/CNFs-900, respectively.

Preparation of hierarchical Ni/Ni_3S_2/CNFs

In a typical hydrothermal procedure, 40 mg of thioacetamide was added into 40 mL of ethanol. After magnetic stirring for 15 min, 18 mg of Ni/CNFs was dispersed in the solution and kept in an autoclave at 120 °C for 4 h. Finally, hierarchical Ni/Ni_3S_2/CNFs were collected by centrifugation, rinsed with ethanol several times, and dried at 50 °C for 12 h. The samples derived from Ni/CNFs-500, Ni/CNFs-700 and Ni/CNFs-900 were named Ni/Ni_3S_2/CNFs-500, Ni/Ni_3S_2/CNFs-700, Ni/Ni_3S_2/CNFs-900, respectively. In addition, a sample of MOF derived Ni/Ni_3S_2 was prepared using a similar procedure but without the addition of PPNF during the template growth of the MOF process. A not-MOF derived Ni/NiS_2/CNFs sample was also prepared using a similar procedure but without the addition of H_2BDC during the template growth of the MOF process.

Electrochemical measurements

An electrochemical workstation (CHI660E Shanghai Chenhua instrument Co., Ltd) was employed for the measurements of cyclic voltammetry (CV), galvanostatic charge–discharge (GCD), and electrochemical impedance spectroscopy (EIS). For tests in a three-electrode system, a platinum foil electrode (20 × 20 × 1.5 mm), a Hg/HgO electrode, Ni foam, and 3 M KOH solution were selected for the counter electrode, reference electrode, current collector, and electrolyte, respectively. The manufacture of the working electrode was illustrated in detail. The ground powder samples (8 mg) were fully mixed with acetylene black (1 mg) and PTFE (1 mg). Then, a few drops of ethanol were added into the mixture to form a paste which was smeared on nickel foam. After drying at 50 °C overnight and being pressed, the electrode can be used for testing. Besides, the fabrication process of electrodes in the two-electrode system is analogous to the working electrodes, but nickel foam was replaced by carbon cloth. PVA–KOH as the solid-state electrolyte was prepared as follows. 3.0 g of PVA was absolutely dissolved in water (30 mL) at a temperature of 90 °C. Next, KOH (3.0 g) was slowly added into the transparent solution at room temperature. After stirring for two hours, the Ni/Ni_3S_2/CNFs and active carbon electrodes were coated with a PVA–KOH gel and dried at room temperature until totally solidified.

Characterization

The morphologies of the samples were characterized using a field-emission scanning electron microscope (FESEM, FEI Nova NanoSEM 450) and a transmission electron microscope (TEM, JEOL JEM-1200 EX) operated at 15 and 100 kV, respectively. TEM combined with high resolution TEM (HRTEM), energy

dispersive X-ray (EDX) spectroscopy and fast Fourier transform (FFT) versions for the existence of Ni_3S_2 was carried out on a FEI Tecnai G2 F20 instrument. The crystal structure and chemical composition of the as-prepared samples were confirmed by powder X-ray diffraction (XRD) patterns with Cu Kα radiation and X-ray photoelectron spectroscopy (XPS, Thermo Scientific ESCALAB250) analysis. Raman spectra were measured on a Horiba Lab RAM HR Evolution apparatus at an excitation wavelength of 532 nm.

Results and discussion

The synthetic process of MOF derived hierarchical Ni/Ni_3S_2/CNFs is schematically illustrated in Scheme 1. And the detailed conversion process of the sample can be predicted. First, PPNFs are obtained through an electrospinning and preoxidation process. Second, Ni ions will penetrate and link to the functional groups of PPNF after being mixed with $Ni(NO_3)_2$, which can be coordinated with organic ligands H_2BDC for the template growth of MOFs on the surface of PPNFs, resulting in a PPNF@MOF sample with a core–shell structure. Third, hierarchical Ni/CNFs were prepared *via* a carbonization process of the PPNF@MOF samples in argon. Finally, hierarchical Ni/Ni_2S_3/CNFs were obtained through the sulfurization reaction between Ni/CNFs and thioacetamide. The relevant reactions are shown below.

$$CH_3CSNH_2 + 2H_2O \rightarrow H_2S + CH_3COONH_4$$

$$3Ni + 2H_2S \rightarrow Ni_3S_2 + 2H_2$$

Morphologies of the as-prepared samples are revealed by SEM and TEM images. Fig. S1 (ESI†) shows a typical SEM image of the prepared PPNF@MOF, showing that flower-like Ni-MOF materials which are composed of tens of nanosheets homogeneously grow on PPNFs with diameters ranging from 180 to 350 nm. And the thickness of the Ni-MOF nanosheet is about 50 nm. As exhibited in Fig. 1a and b, after calcination at 700 °C in Ar for 2 h, the diameters of the prepared Ni/CNFs-700 are slightly reduced, and the shape of the MOF-derived Ni-carbon backbone looks like a carnation flower. Similarly, the prepared Ni/CNFs-500 maintains well the morphology of the Ni/CNFs-700 (Fig. S2a and b, ESI†). However, when the carbonization temperature increases to 900 °C, the flower morphology of the obtained Ni/CNFs-900 sample is destroyed and some Ni-carbon particles are separated from CNFs. In addition, the well-preserved CNFs reveal that the carbon derived from PAN possesses more stable structures than the carbon converted from organic ligands. After the sulfurization process, carnation-like Ni-carbon materials are partially turned into raspberry-like Ni_3S_2-carbon materials which are exhibited in Fig. 1c and d. Compared with the morphologies of Ni/Ni_3S_2/CNFs-500 (Fig. S2c and d, ESI†) and Ni/Ni_3S_2/CNFs-900

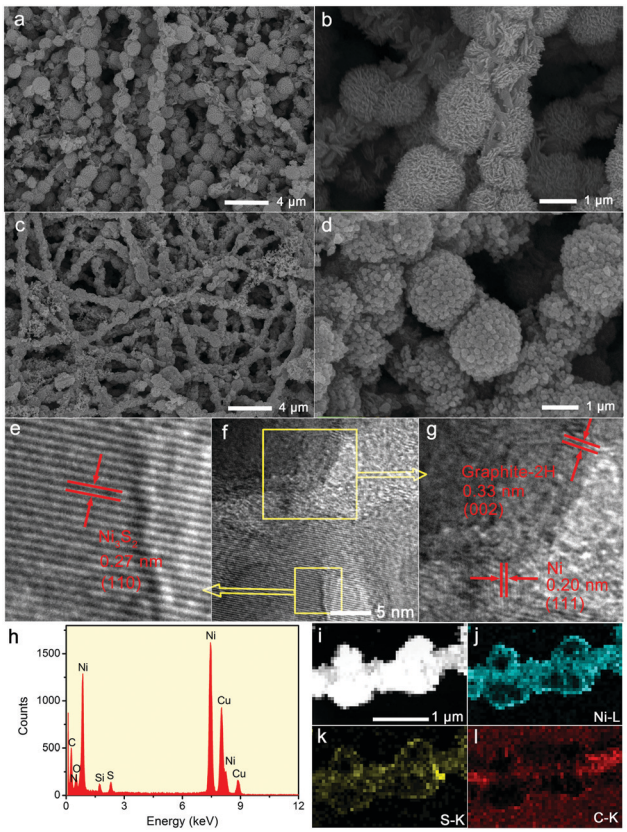

Fig. 1 SEM images of (a and b) Ni/CNFs-700 and (c and d) Ni/Ni_3S_2/CNFs-700 with different magnifications. (e–g) HRTEM images, (h) EDX spectrum, (i) HAADF-STEM, EDX elemental mapping of (j) Ni–L, (k) S–K, and (l) C–K of Ni/Ni_3S_2/CNFs-700.

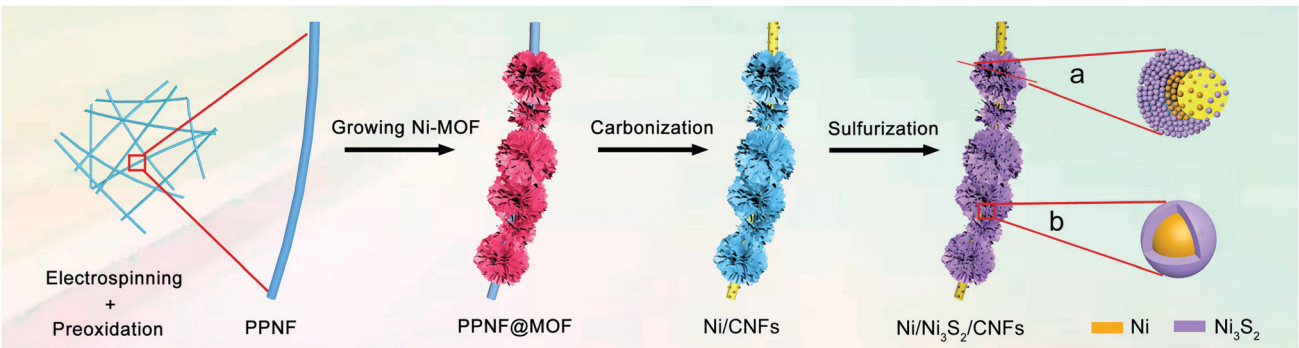

Scheme 1 Schematic demonstration of the fabrication process of MOF derived hierarchical Ni/Ni_3S_2/CNFs.

(Fig. S2g and h, ESI†), it seems that a looser structure is obtained in the Ni/Ni_3S_2/CNFs-700 sample, which may bring about more exposed active sites and better electrochemical performance. In addition, from the TEM images of PPNF@MOF, Ni/CNFs, and Ni/Ni_3S_2/CNFs (Fig. S3a–c, ESI†), it is found that all the samples present core–shell structures. HRTEM results are carried out to confirm the crystal type of nickel sulfide for the as-prepared Ni/Ni_3S_2/CNFs-700 sample. Fig. 1e intercepted from Fig. 1f illustrates an obvious lattice fringe of 0.28 nm, which is ascribed to the (110) crystal plane of Ni_3S_2. In particular, the lattice fringes of 0.33 nm in Fig. 1g that surround the Ni_3S_2 nanoparticles are assigned to the (002) crystal plane of graphitic carbon, revealing that the nickel species can effectively catalyze the graphitization of carbon during the carbonization process. Meanwhile, the lattice fringe of 0.2 nm of Ni is observed in Fig. 1g, which can be explained as the incomplete sulfurization of Ni/CNFs-700 due to the protection of carbon. Energy dispersive X-ray spectroscopy is performed to investigate the elemental composition of the Ni/Ni_3S_2/CNFs-700 sample. The signals of S, Ni, C, O and N observed from Fig. 1h correspond to the detected Ni_3S_2 in the product. Besides, the signals of Cu and Si are related to the copper mesh and the instrument. Fig. 1i shows the HAADF-STEM image of the Ni/Ni_3S_2/CNFs-700 sample, and its EDX mappings (Fig. 1j–l) display a uniform distribution of the Ni element throughout the sample; however, element S is dominant outside the sample compared with the Ni element, revealing that the MOF shell is fully sulfurized while the Ni particles within CNFs are not easily sulfurized due to the restriction of the MOF shell. Besides, the C element mapping demonstrates a more dense distribution in the core because of the lower carbon content derived from the organic ligand in the MOF than PAN.

XRD patterns are carried out to explore the crystal phase of the prepared samples. As demonstrated in Fig. S4 (ESI†), after calcination at 700 °C, PPNF@MOF was converted into Ni/CNFs. The typical diffraction peaks (2θ) located at 44.5°, 51.9°, and 76.4° can be ascribed to the (111), (200) and (220) crystal planes of the face-centered-cubic phase of Ni (JCPDS no. 04-0850). Fig. S5 (ESI†) shows the XRD patterns of Ni/CNFs-500 and Ni/CNFs-900, whose peaks are in accordance with that of Ni/CNFs-700. But their intensity increases with increasing calcination temperature, revealing that the crystallization degree of nickel also increases. After sulfurization, some new distinct diffraction peaks (2θ) at 21.8°, 31.1°, 44.3°, and 50.1° can be detected in the XRD patterns of Ni/Ni_3S_2/CNFs, which are assigned to the (101), (110), (202), and (211) crystal planes of Ni_3S_2 (JCPDS no. 44-1418), respectively (Fig. 2a). Specifically, all the samples still show the characteristic Ni patterns, which could be owing to incomplete sulfurization of Ni nanoparticles. There are two speculations to explain this phenomenon (Scheme 1). On the one hand, the Ni particles within Ni/CNFs cannot be sulfurized due to the protection of the MOF which resists sulfur ion penetrating into the core material. On the other hand, the sulfurization process only occurs on the surface of some nickel particles, which is related to their higher crystallinity and larger diameters. Furthermore, XRD patterns of the MOF derived Ni/Ni_3S_2 exhibited similar patterns to those of

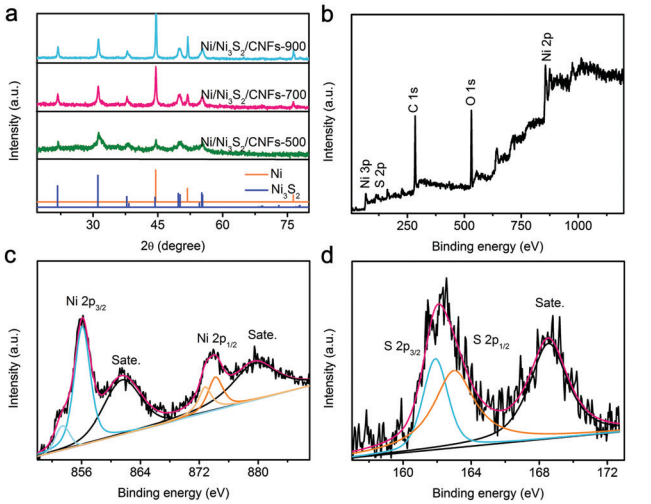

Fig. 2 (a) XRD patterns of Ni/Ni_3S_2/CNFs-500, Ni/Ni_3S_2/CNFs-700 and Ni/Ni_3S_2/CNFs-900. (b) XPS survey scan spectrum and high-resolution spectra of (c) Ni 2p peaks and (d) S 2p peaks for the Ni/Ni_3S_2/CNFs-700 sample.

Ni/Ni_3S_2/CNFs, while the not-MOF derived Ni/NiS_2/CNFs show very weak NiS_2 peaks. This result implies that Ni-CNFs derived from MOFs are easier to convert to Ni_3S_2 than Ni-CNFs derived from not-MOF materials. The Raman spectra and corresponding fitting curves of Ni/Ni_3S_2/CNFs-700, Ni/Ni_3S_2/CNFs-500 and PPNF@MOF are presented in Fig. S6 (ESI†). The intensity ratio of the D peak to the G peak (I_D/I_G) of Ni/Ni_3S_2/CNFs-700, Ni/Ni_3S_2/CNFs-500 and PPNF@MOF is calculated to be 1.03, 1.28, and 1.42, respectively. The lower I_D/I_G reflects the higher graphitization degree of Ni/Ni_3S_2/CNFs-700 than Ni/Ni_3S_2/CNFs-500, which is consistent with the results in previous work.[28] In addition, compared with the I_D/I_G of PPNF@MOF, it can be inferred that the graphitization degree of the precursor can be greatly improved *via* the calcination at 500 °C and 700 °C.

XPS analysis is further implemented to investigate the chemical states of Ni/Ni_3S_2/CNFs-700. From Fig. 2b, the characteristic peaks in the full survey scan spectrum confirm the existence of C, O, S and Ni elements. The Ni 2p spectrum is fitted into two spin–orbit doublets followed by two shake-up satellites. The peaks with binding energies at 853. 3 eV for Ni $2p_{3/2}$ and 872.8 eV for Ni $2p_{1/2}$ correspond to the spin–orbit characteristics of Ni^{2+}, and the binding energies centered at 856.1 eV for Ni $2p_{3/2}$ and 874.2 eV for Ni $2p_{1/2}$ belong to the characteristics of Ni^{3+}.[29–31] Two shake-up typical peaks of nickel appear at the high binding energy sides of Ni $2p_{3/2}$ and Ni $2p_{1/2}$. Fig. 2d displays the high-resolution S 2p spectrum which can be deconvoluted into two main peaks and a satellite. The peaks located at binding energies of 161.9 eV and 163.0 eV are indexed to S $2p_{3/2}$ and S $2p_{1/2}$, which are explained as S^{2-} with low surface coordination and sulfur–metal bonds, respectively. In addition, the S 2p peak at around 168.6 eV is attributed to the surface sulfur species at certain higher oxidation states.[31–34] These results agree well with the HR-TEM, EDX and XRD analysis.

The electrochemical performance of the as-fabricated electrodes is tested in a three electrode system using 3 M KOH as

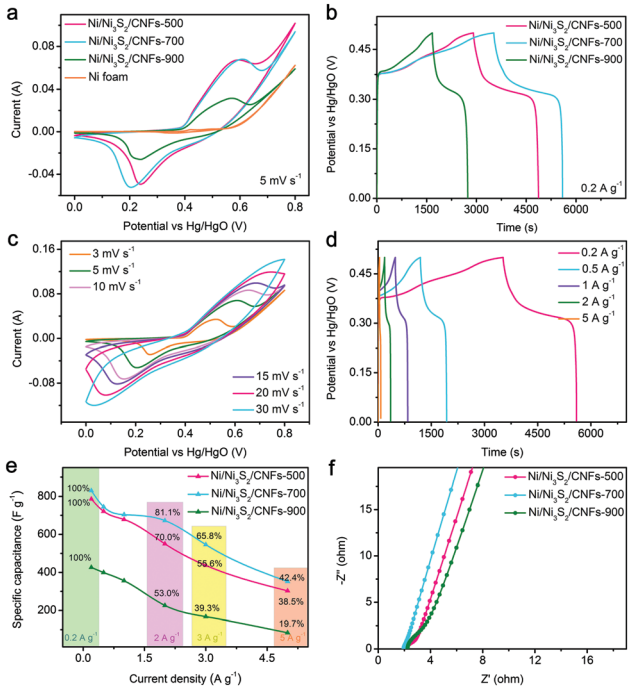

Fig. 3 (a) CV curves of the Ni/Ni_3S_2/CNFs-500, Ni/Ni_3S_2/CNFs-700, Ni/Ni_3S_2/CNFs-900 electrodes, and Ni foam at 5 mV s^{-1}. (b) GCD curves of the Ni/Ni_3S_2/CNFs-500, Ni/Ni_3S_2/CNFs-700, and Ni/Ni_3S_2/CNFs-900 electrodes at 0.2 A g^{-1}. (c) CV curves of the Ni/Ni_3S_2/CNFs-700 electrode at different scan rates and (d) GCD curves of the Ni/Ni_3S_2/CNFs-700 electrode at various current densities. (e) Specific capacitance and capacitance retention at different current densities, and (f) Nyquist plots of the Ni/Ni_3S_2/CNFs-500, Ni/Ni_3S_2/CNFs-700, and Ni/Ni_3S_2/CNFs-900 electrodes.

the electrolyte. The influence of calcination temperature on electrochemical performance is investigated. In detail, as illustrated in Fig. 3a, one clear redox peak pair between 0.1 and 0.7 V appears in the CV curves of the Ni/Ni_3S_2/CNFs-500, Ni/Ni_3S_2/CNFs-700 and Ni/Ni_3S_2/CNFs-900 electrodes at a scan rate of 5 mV s^{-1}, corresponding to the associated redox reactions of Ni^{2+}/Ni^{3+} as shown below.

$$Ni_3S_2 + 3OH^- \leftrightarrow Ni_3S_2(OH)_3 + 3e^-.$$

In addition, according to the areas enclosed by the CV curves, it can be evaluated that the capacity of the Ni/Ni_3S_2/CNFs-700 electrode is larger than those of the Ni/Ni_3S_2/CNFs-500 and Ni/Ni_3S_2/CNFs-900 electrodes, which may stem from the synergistic effect of improved conductivity and large active surface area. Their specific capacitance can be obtained on the basis of GCD curves and the following formula:

$$C_g = (I\Delta t)/(m\Delta V)$$

where C_g, I, Δt, m, and ΔV correspond to the specific capacitance (F g^{-1}) of the electrode, the discharge current (A), the discharge time (s), the mass of hybrids (g), and the applied potential range (V), respectively.

From Fig. 3b, the specific capacitance of the Ni/Ni_3S_2/CNFs-500, Ni/Ni_3S_2/CNFs-700, and Ni/Ni_3S_2/CNFs-900 electrodes at 0.2 A g^{-1} is calculated to be 785.8, 830.0, and 426.5 F g^{-1}, respectively, consistent with the results presented by the CV curves. Notably, because of the electrochemical polarization of the electrode material, the voltage range of the GCD curves deviates from that of the CV curves.[35,36] Fig. 3c displays CV curves at different scan rates ranging from 3 to 30 mV s^{-1} for the Ni/Ni_3S_2/CNFs-700 electrode. As the scan rate increases, the symmetric shape of the oxidation peak and reduction peak is well maintained, which is recorded to understand the good reversibility of electrodes. The redox peak shifts in their respective directions due to the increment in mass transport resistance.[37] On the basis of GCD curves in Fig. 3d, the specific capacitance of the Ni/Ni_3S_2/CNFs-700 electrode is 744.5, 704.0, 672.8, and 352.0 F g^{-1} at densities of 0.5, 1, 2, and 5 A g^{-1}. A detailed comparison of specific capacitance and capacitance retention at different densities for different electrodes are shown in Fig. 3e. When the current density is increased by 25 times, the specific capacitance can still maintain 42.4% of the original value, which is higher than 38.5% of the value of Ni/Ni_3S_2/CNFs-500, 19.7% of Ni/Ni_3S_2/CNFs-900 and some typical materials reported in previous literature, such as PPNF@Ni-MOF (from 0.5 to 5 A g^{-1}, 42.9%);[28] Co_9S_8/RGO/Ni_3S_2 on Ni foam (from 3.9 to 15.6 A g^{-1}, 69.5%);[38] hollow NiS_x microspheres (from 0.5 to 8.0 A g^{-1}, 20.4%);[39] and NiMn-LDH nanosheet@Ni_3S_2 nanorod (from 3 to 20 A g^{-1}, 68.3%).[40]

Electrochemical impedance spectroscopy (EIS) analysis is employed to understand the high performance of Ni/Ni_3S_2/CNFs-700. The Nyquist plots in Fig. 3f are tested within the frequency ranges from 0.01 Hz to 10^5 Hz. Charge-transfer impedance is represented by the semicircle in the high frequency region of the Nyquist plot, occurring on the electrode–electrolyte interface of the electrode. Smaller radius can be explained as lower charge transfer resistance, leading to the better rate performance of the Ni/Ni_3S_2/CNFs-700 electrode than other electrodes.[41,42] And the lower ion transfer resistance of the Ni/Ni_3S_2/CNFs-700 electrode can be verified by the larger slope of inclined lines in the low frequency region, which is a key factor for high capacitance.[43] These results reveal that the superior performance of Ni/Ni_3S_2/CNFs-700 to Ni/Ni_3S_2/CNFs-500 and Ni/Ni_3S_2/CNFs-900 electrodes benefits from the optimum degree of calcination of precursors. First, compared with Ni/CNFs-900, Ni/CNFs-700 with well-preserved morphologies as a template not only is conducive to making contact with sulfur sources but also provides a larger interface area between Ni/Ni_3S_2/CNFs-700 and KOH. Second, the higher degree of carbonization leads to better conductivity of Ni/Ni_3S_2/CNFs-700 than Ni/Ni_3S_2/CNFs-500, which is beneficial to the fast electron transport. In addition, the crystallization and particle size of nickel determine the sulfurization degree of the materials, further affecting their electrochemical behaviors.

The samples of Ni/CNFs-700, MOF derived Ni/Ni_3S_2 and not-MOF derived Ni/NiS_2/CNFs are prepared to evaluate the effects of the core–shell structure and sulfurization on the electrochemical behaviors of Ni/Ni_3S_2/CNFs-700. Fig. 4a shows the CV measurements of the Ni/Ni_3S_2/CNFs-700, Ni/CNFs-700, MOF derived Ni/Ni_3S_2 and not-MOF derived Ni/NiS_2/CNFs electrodes at a constant scan rate of 5 mV s^{-1}. It is found that

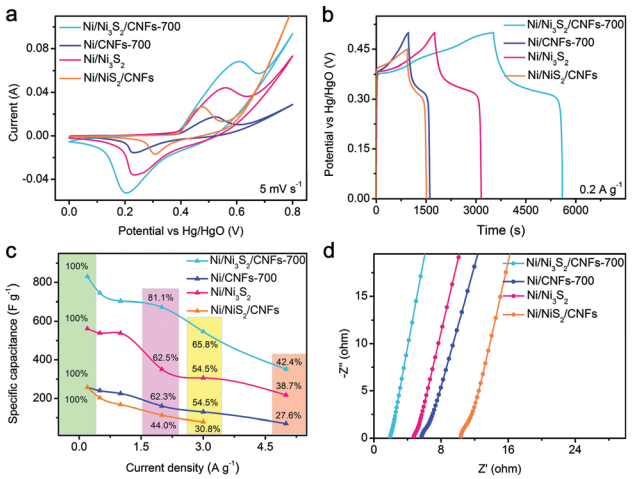

Fig. 4 (a) CV curves at a scan rate of 5 mV s^{-1} and (b) GCD curves at a current density of 0.2 A g^{-1}, (c) specific capacitance and capacitance retention at different current densities, (d) Nyquist plots of the Ni/Ni_3S_2/CNFs-700, Ni/CNFs-700, MOF derived Ni/Ni_3S_2 and not-MOF derived Ni/NiS_2/CNFs electrodes.

the Ni/Ni_3S_2/CNFs-700 electrode delivers much larger capacitance than the Ni/CNFs-700 electrode, suggesting that the conversion from nickel to nickel sulfide contributes significantly to the capacity of the samples. As illustrated in Fig. 4b, charging and discharging platforms of four electrodes are associated with their corresponding redox reactions of Ni^{2+}/Ni^{3+}. When the current density is 0.2 A g^{-1}, the specific capacitances of the Ni/CNFs-700, MOF derived Ni/Ni_3S_2 and not-MOF derived Ni/NiS_2/CNFs electrodes are 257.5, 561.8, and 257.2 F g^{-1}. The Ni/Ni_3S_2/CNFs-700 electrode possesses higher capacitance than both MOF derived Ni/Ni_3S_2 and not-MOF derived Ni/NiS_2/CNFs, from which it can be inferred that the construction of the core–shell structure is beneficial to the increment of their electrochemical properties. Furthermore, the Ni/Ni_3S_2/CNFs-700 electrode exhibits a superior rate capacity over other electrodes (Fig. 4c). In particular, the introduction of nickel sulfide particles into carbon nanofibers not only plays an important role in the improved capacitance, but also helps in the improvement of the rate performance, which may be resulting from their relatively large redox active interface area and high conductivity.

Fig. 4d shows that both the Ni_3S_2 and core–shell structure of the Ni/Ni_3S_2/CNFs-700 sample synergistically facilitate the charge transfer and electrolyte diffusion into the electrode material. On the one hand, Ni_3S_2 with superior intrinsic electronic properties closely combines with conductive carbon materials, providing a large number of redox active sites and smooth channels for electrons. On the other hand, the core–shell structure constructs a high electrolyte/electrode interface area, resulting in efficient ion diffusion. These characteristics contribute to the improved electrochemical performance to some degree.

An asymmetric solid-state supercapacitor is assembled to further investigate the potential practical application of the Ni/Ni_3S_2/CNFs-700 materials. The loading mass ratio of Ni/Ni_3S_2/CNFs-700 to AC is estimated to be 1 : 4.4 in light of the results exhibited in Fig. S7 (ESI†). Fig. 5a schematically demonstrates

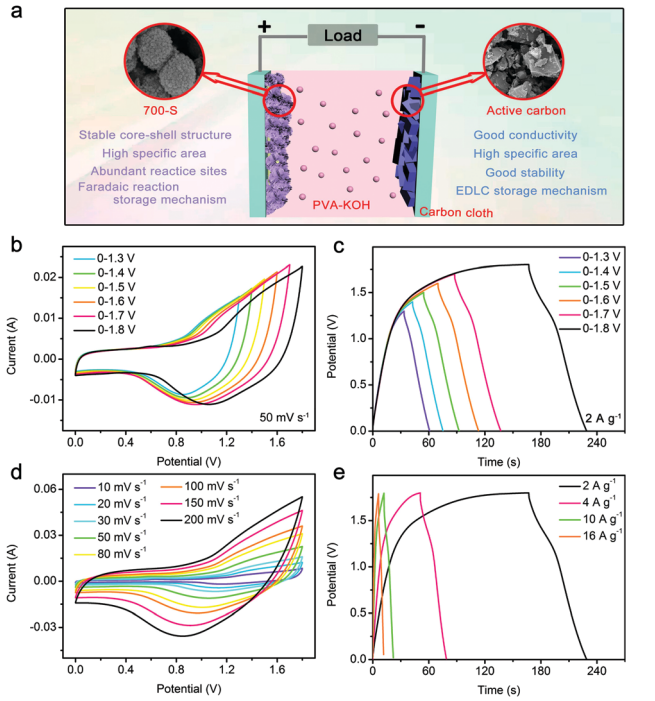

Fig. 5 (a) Schematic representation of the construction of an asymmetric solid-state supercapacitor using Ni/Ni_3S_2/CNFs-700 as the positive electrode material and active carbon as the negative electrode material. (b) CV curves at 50 mV^{-1} and (c) GCD curves at 2 A g^{-1} within different potential windows, (d) CV curves at different scan rates and (e) GCD curves at various current densities within the potential window of 0–1.8 V of the ASC device.

the construction of the asymmetric solid-state supercapacitor (ASC). PVA-KOH and carbon cloth are used as the electrolyte and current collector, respectively. CV curves at a scan rate of 50 mV s^{-1} and GV curves at a current density of 2 A g^{-1} are measured within different potential windows. From Fig. 5b and c, it is noticed that the voltage range can be extended to 1.8 V because of the application of solid electrolytes.[44,45] And as the voltage range expands, the capacitance of the device is improved. The specific capacitance of the ASC is obtained according to the following formula:

$$C_{cell} = (I\Delta t)/(m_{total}\Delta V)$$

where C_{cell} and m_{total} refer to the specific capacitance (F g^{-1}) of the solid-state ASC and the total mass (g) of two electrodes.

Referring to Fig. 5c, the specific capacitance with voltage windows of 0–1.3, 0–1.4, 0–1.5, 0–1.6, 0–1.7 and 0–1.8 V is calculated to be 43.6, 47.6, 52.7, 54.4, 58.8, and 70.2 F g^{-1}, respectively. In addition, CV measurements at different scan rates and GV measurements at various current densities are explored in the potential range of 0–1.8 V. There is no distinct deformation for the shape of CV curves with the increase of scan rate, indicating the fast charging/discharging process of the ASC. The energy density and power density of the ASC can be calculated based on its specific capacitance at different current densities and the following formula.

$$E = 1/2C_{cell}\Delta V^2$$

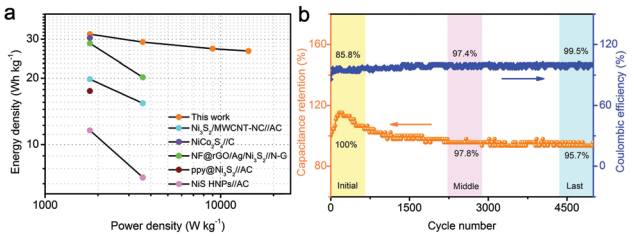

Fig. 6 (a) Ragone plots (energy density *vs.* power density), (b) the cycling stability and Coulombic efficiency of the as-assembled ASC devices.

$$P = E/t$$

where E and P represent the energy density (W h kg^{-1}) and power density (W kg^{-1}) of the solid-state ASC, respectively.

Ragone plots of energy density *vs.* power density are depicted in Fig. 6a. The ASC delivers the highest energy density of 31.6 W h kg^{-1} at 2 A g^{-1} with a power density of 1800 W kg^{-1}. When the current density is increased to 16 A g^{-1}, the maximum power density of 14 400 W kg^{-1} is achieved, and the energy density can still be maintained at around 26.5 W h kg^{-1}. The high energy density is related to the high specific capacitance of Ni/Ni_3S_2/CNFs-700 and the sufficient power from active carbon. This good performance is better than the performance reported in previous similar works on asymmetric supercapacitors, including Ni_3S_2/MWCNT-NC//AC (19.8 W h kg^{-1}, 798 W kg^{-1});[13] $NiCo_2S_4$@NiO//AC (30.4 W h kg^{-1}, 288 W kg^{-1});[46] NF@rGO/Ag/Ni_3S_2//N-G ASC (28.7 W h kg^{-1}, 425 W kg^{-1});[47] ppy@Ni_3S_2//AC (17.5 W h kg^{-1}, 179.3 W kg^{-1});[48] and NiS HNPs//AC (11.6 W h kg^{-1}, 187.5 W kg^{-1}).[49]

Cycling stability is another important factor for practical application of supercapacitors. Fig. 6b shows the capacitance retention and corresponding Coulombic efficiency of the Ni/Ni_3S_2/CNFs//AC ASC device at a current density of 2 A g^{-1}. For the first 400 cycles, because of the activation of the electrode material, the capacitance is on the rise and the Coulombic efficiency gradually stabilizes to be around 93.5%. After 5000 charge and discharge cycles, capacitance can still maintain 95.7% of the initial value and the Coulombic efficiency reaches 99.5% of the initial value, indicating the good cycling stability and reversibility.[50,51]

Conclusions

In summary, we have designed and prepared novel hierarchical Ni/Ni_3S_2 decorated CNFs through the template growth of MOF on PPNFs followed by carbonization and sulfurization processes. The obtained Ni/Ni_3S_2/CNFs electrode displays a high specific capacitance of 830.0 F g^{-1} at 0.2 A g^{-1} and excellent rate performance, which are attributed not only to the superior pseudocapacitance of Ni_3S_2 and the high conductivity of Ni/CNFs, but also to the large active interface area provided by the MOF on the PPNF derived core–shell structure. In addition, an asymmetric solid-state supercapacitor is assembled with a high energy of 31.6 W h kg^{-1} at a power density of 1800 W kg^{-1} and good cycling stability over 5000 cycles.

Conflicts of interest

There are no conflicts to declare.

Acknowledgements

This work was financially supported by the National Natural Science Foundation of China (21875084, 51773075) and the Project of Science and Technology Agency, Jilin Province (20190101013JH).

References

1 X. Lu, C. Wang, F. Favier and N. Pinna, *Adv. Energy Mater.*, 2017, **7**, 1601301.
2 A. T. E. Vilian, B. Dinesh, M. Rethinasabapathy, S. K. Hwang, Ch. S. Jin, Y. S. Huh and Y. K. Han, *J. Mater. Chem. A*, 2018, **6**, 14367–14379.
3 X. Han, Y. Yang, J. Zhou, Q. Ma, K. Tao and L. Han, *Chem. – Eur. J.*, 2018, **24**, 1–10.
4 L. Liu, Y. Yan, Z. Cai, S. Lin and X. Hu, *Adv. Mater. Interfaces*, 2018, **5**, 1701548.
5 C. Qu, Z. Liang, Y. Jiao, B. Zhao, B. Zhu, D. Dang, S. Dai, Y. Chen, R. Zou and M. Liu, *Small*, 2018, **14**, 1800285.
6 J. S. Chen, C. Guan, Y. Gui and D. J. Blackwood, *ACS Appl. Mater. Interfaces*, 2017, **9**, 496–504.
7 B. Li, M. Zheng, H. Xue and H. Pang, *Inorg. Chem. Front.*, 2016, **3**, 175–202.
8 H. Huo, Y. Zhao and C. Xu, *J. Mater. Chem. A*, 2014, **2**, 15111–15117.
9 L. Mi, Q. Ding, W. Chen, L. Zhao, H. Hou, C. Liu, C. Shen and Z. Zheng, *Dalton Trans.*, 2013, **42**, 5724–5730.
10 J. Zhu, S. P. Jiang, R. Wang, K. Shic and P. K. Shen, *J. Mater. Chem. A*, 2014, **2**, 15448–15453.
11 W. He, C. Wang, H. Li, X. Deng, X. Xu and T. Zhai, *Adv. Energy Mater.*, 2017, **7**, 1700983.
12 T. Li, Y. Zuo, X. Lei, N. Li, J. Liu and H. Han, *J. Mater. Chem. A*, 2016, **4**, 8029–8040.
13 C. S. Dai, P. Y. Chien, J. Y. Lin, S. W. Chou, W. K. Wu, P. H. Li, K. Y. Wu and T. W. Lin, *ACS Appl. Mater. Interfaces*, 2013, **5**, 12168–12174.
14 W. Du, Y. L. Bai, J. Xu, H. Zhao, L. Zhang, X. Li and J. Zhang, *J. Power Sources*, 2018, **402**, 281–295.
15 C. Wang, Y. V. Kaneti, Y. Bando, J. Lin, C. Liu, J. Li and Y. Yamauchi, *Mater. Horiz.*, 2018, **5**, 394–407.
16 W. Zhao, J. Peng, W. Wang, S. Liu, Q. Zhao and W. Huang, *Coord. Chem. Rev.*, 2018, **377**, 44–63.
17 S. Sundriyal, H. Kaur, S. K. Bhardwaj, S. Mishra, K. H. Kim and A. Deep, *Coord. Chem. Rev.*, 2018, **369**, 15–38.
18 Y. L. Li, J. J. Zhou, M. K. Wu, C. Chen, K. Tao, F. Y. Yi and L. Han, *Inorg. Chem.*, 2018, **57**, 6202–6205.
19 K. Rui, X. Wang, M. Du, Y. Zhang, Q. Wang, Z. Ma, Q. Zhang, D. Li, X. Huang, G. Sun, J. Zhu and W. Huang, *ACS Appl. Mater. Interfaces*, 2018, **10**, 2837–2842.
20 K. Qi, R. Hou, S. Zaman, Y. Qiu, B. Y. Xia and H. Duan, *ACS Appl. Mater. Interfaces*, 2018, **10**, 18021–18028.

21 C. Qu, Z. Liang, Y. Jiao, B. Zhao, B. Zhu, D. Dang, S. Dai, Y. Chen, R. Zou and M. Liu, *Small*, 2018, **14**, 1800285.
22 Y. Huang, L. Quan, T. Liu, Q. Chen, D. Cai and H. Zhan, *Nanoscale*, 2018, **10**, 14171–14181.
23 X. Liu, W. Zang, C. Guan, L. Zhang, Y. Qian, A. M. Elshahawy, D. Zhao, S. J. Pennycook and J. Wang, *ACS Energy Lett.*, 2018, **3**, 2462–2469.
24 C. Qu, L. Zhang, W. Meng, Z. Liang, B. Zhu, D. Dang, S. Dai, B. Zhao, H. Tabassum, S. Gao, H. Zhang, W. Guo, R. Zhao, X. Huang, M. Liu and R. Zou, *J. Mater. Chem. A*, 2018, **6**, 4003–4012.
25 Y. Su, S. Li, D. He, D. Yu, F. Liu, N. Shao and Z. Zhang, *ACS Sustainable Chem. Eng.*, 2018, **6**, 11989–11998.
26 Y. Zhang, H. Chen, C. Guan, Y. Wu, C. Yang, Z. Shen and Q. Zou, *ACS Appl. Mater. Interfaces*, 2018, **10**, 18440–18444.
27 J. Zhao, H. Li, C. Li, Q. Zhang, J. Sun, X. Wang, J. Guo, L. Xie, J. Xie, B. He, Z. Zhou, C. Lu, W. Lu, G. Zhu and Y. Yao, *Nano Energy*, 2018, **45**, 420–431.
28 D. Tian, X. Lu, Y. Zhu, M. Li and C. Wang, *J. Power Sources*, 2019, **413**, 50–58.
29 C. Zhang, Y. Huang, S. Tang, M. Deng and Y. Du, *ACS Energy Lett.*, 2017, **2**, 759–768.
30 W. Wei, L. Mi, Y. Gao, Z. Zheng, W. Chen and X. Guan, *Chem. Mater.*, 2014, **26**, 3418–3426.
31 W. He, C. Wang, H. Li, X. Deng, X. Xu and T. Zhai, *Adv. Energy Mater.*, 2017, **7**, 1700983.
32 X. Wang, B. Shi, X. Wang, J. Gao, C. Zhang, Z. Yang and H. Xie, *J. Mater. Chem. A*, 2017, **5**, 23543–23549.
33 X. Liu, Y. Li, N. Chen, D. Deng, X. Xing and Y. Wang, *Electrochim. Acta*, 2016, **213**, 730–739.
34 J. Wen, S. Li, K. Zhou, Z. Song, B. Li, Z. Chen, T. Chen, Y. Guo and G. Fang, *J. Power Sources*, 2016, **324**, 325–333.
35 S. Liu, S. C. Lee, U. M. Patil, C. Ray, K. V. Sankar, K. Zhang, A. Kundu, S. Kang, J. H. Parkc and S. C. Jun, *J. Mater. Chem. A*, 2017, **5**, 4543–4549.
36 A. S. Hameed, *Phosphate Based Cathodes and Reduced Graphene Oxide Composite Anodes for Energy Storage Applications*, Springer, 2016.
37 X. Xiong, B. Zhao, D. Ding, D. Chen, C. Yang, Y. Lei and M. Liu, *NPG Asia Mater.*, 2016, **8**, 1–7.
38 Z. Zhang, Q. Wang, C. Zhao, S. Min and X. Qian, *ACS Appl. Mater. Interfaces*, 2015, **7**, 4861–4868.
39 J. Wang, K. Y. Ma, J. Zhang, F. Liu and J. P. Cheng, *J. Colloid Interface Sci.*, 2017, **507**, 290–299.
40 S. Yu, Y. Zhang, G. Lou, Y. Wu, X. Zhu, H. Chen, Z. Shen, S. Fu, B. Bao and L. Wu, *Sci. Rep.*, 2018, **8**, 5246.
41 G. Zhu, H. Wen, M. Ma, W. Wang, L. Yang, L. Wang, X. Shi, X. Cheng, X. Sun and Y. Yao, *Chem. Commun.*, 2018, **54**, 10499–10502.
42 H. Zhang, B. Xu, Z. Xiao, H. Mei, L. Zhang, Y. Han and D. Sun, *CrystEngComm*, 2018, **20**, 4313–4320.
43 X. M. Cao, Z. J. Sun, S. Y. Zhao, B. Wang and Z. B. Han, *Mater. Chem. Front.*, 2018, **2**, 1692–1699.
44 L. Zhang, P. Zhu, F. Zhou, W. Zeng, H. Su, G. Li, J. Gao, R. Sun and C. Wong, *ACS Nano*, 2016, **10**, 1273–1282.
45 D. Tian, X. Lu, G. Nie, M. Gao and C. Wang, *Inorg. Chem. Front.*, 2018, **5**, 635–642.
46 Y. Huang, T. Shi, S. Jiang, S. Cheng, X. Tao, Y. Zhong, G. Liao and Z. Tang, *Sci. Rep.*, 2016, **6**, 38620.
47 J. Qi, Y. Chang, Y. Sui, Y. He, Q. Meng, F. Wei, Y. Ren and Y. Jin, *Adv. Mater. Interfaces*, 2018, **5**, 1700985.
48 L. Long, Y. Yao, M. Yan, H. Wang, G. Zhang, M. Kong, L. Yang, X. Liao, G. Yin and Z. Huang, *J. Mater. Sci.*, 2017, **52**, 3642–3656.
49 Z. Li, X. Yu, A. Gu, H. Tang, L. Wang and Z. Lou, *Nanotechnology*, 2017, **28**, 065406.
50 D. Tian, X. Lu, G. Nie, M. Gao, N. Song and C. Wang, *Appl. Surf. Sci.*, 2018, **458**, 389–396.
51 Z. Tang, C. Tang and H. Gong, *Adv. Funct. Mater.*, 2012, **22**, 1272–1278.

